Attaining the ground state of kagome artificial spin ice via ultrafast site-specific laser annealing

D. Pecchio, S. Sahoo,* V. Scagnoli,† and L. J. Heyderman‡
Laboratory for Mesoscopic Systems, Department of Materials, ETH Zurich, 8093 Zurich, Switzerland and PSI Center for Neutron and Muon Sciences, 5232 Villigen PSI, Switzerland

(Received 2 October 2025; revised 8 January 2026; accepted 12 January 2026; published 20 February 2026)

Artificial spin ices (ASIs) provide a versatile platform to explore magnetic frustration and emergent phenomena. However, in kagome ASI, experimental access to the ground state remains elusive due to dynamical freezing. Here we demonstrate a deterministic and rewritable approach to attain the ground state using ultrafast, site-selective laser annealing. By engineering sublattice-dependent optical absorption through selective capping of the nanomagnets with Cr or utilizing different nanomagnet thicknesses, we achieve selective partial demagnetization and subsequent reversal of one nanomagnet sublattice under a subcoercive magnetic field, driving the system into the ground state in a single switching step. Magnetic force microscopy reveals nearly perfect long-range ordering, while heat-transfer simulations confirm the sublattice-selective excitation mechanism. This work establishes an ultrafast method to attain the kagome ASI ground state, which does not require a modification of the geometry of the ASI or the materials used for the individual nanomagnets. Beyond ground-state writing, this site-selective activation provides an important tool for controlling the magnetic states, which is important for applications such as reconfigurable magnonic crystals, neuromorphic computing and programmable nanomagnetic logic.

DOI: 10.1103/nl4z-3pn1

I. INTRODUCTION

Artificial spin ices (ASIs) are lithographically patterned arrays of dipolar-coupled, single-domain nanomagnets [1], designed to emulate the magnetic frustration and cooperative behavior observed in geometrically constrained spin systems such as those found in the rare-earth pyrochlores [2]. With the possibility to create various geometries lithographically, and therefore tune the interactions, these magnetic metamaterials provide a versatile platform to explore collective phenomena—such as emergent magnetic monopoles [3,4], phase transitions [5–8], and magnetic frustration [9,10]—in a tailored, reconfigurable, and directly observable setting. Early experimental realizations include both nanomagnet arrays [9,11] and honeycomb nanowire networks [12,13], which established ASI as a platform for directly imaging frustrated microstates.

Among the various ASIs explored, the kagome ASI stands out due to its high degree of magnetic frustration and the resulting manifold of numerous degenerate low-energy microstates [11–16], and a central objective in the study of kagome ASI is to identify and access its various thermodynamic phases [5,6,14,15]. In this ASI, stadium-shaped single-domain nanomagnets, whose magnetic moments are referred to as macrospins, are arranged on hexagonal plaquettes so that three nanomagnets meet at each lattice vertex with an angle between them of 120° [see Figs. 1(a) and 1(b)]. The macrospin associated with each nanomagnet can point in one of two directions parallel to the nanomagnet long axis and can be denoted as pointing in (pointing out) when its magnetization points towards (away from) the vertex. The so-called ice rule refers to the local magnetostatic constraints that must be satisfied at any given vertex, giving the lowest-energy 1-in/2-out or 2-in/1-out configuration, which is sixfold degenerate, while the doubly degenerate all-in (3-in) or all-out (3-out) vertices form high-energy defects. This can be formalized with the dumbbell model [4,17], where each (macro)spin is replaced by a dumbbell with $\pm q$ magnetic poles at its ends. The vertex magnetic charge is then given by $Q = q\sum_i s_i$ with $s_i = +1$ at the vertex for macrospins pointing in and $s_i = -1$ for macrospins pointing out. Ice-rule-obeying vertices therefore carry the minimum charge magnitude $|Q| = q$, whereas ice-rule-violating 3-in/3-out defects have $|Q| = 3q$. Vertices with $|Q| = 3q$ behave as magnetic excitations, commonly referred to as emergent magnetic monopoles in the context of ASI [3,4,18]. Ice-rule-obeying vertices, by contrast, belong to the low-energy manifold. However, when the system is considered relative to the charge-ordered ground state discussed below, any deviations from perfect charge order, which also includes ice-rule-obeying vertices, can be viewed as excitations. The location of such emergent magnetic monopoles becomes clear when considering the smeared magnetic charge density [4].

In terms of the temperature-dependent behavior, theoretical models predict a sequence of magnetic phases in kagome ice on decreasing the temperature [14,15], which are illustrated

*Contact author: sourav.sahoo@psi.ch
†Contact author: valerio.scagnoli@psi.ch
‡Contact author: laura.heyderman@psi.ch

Published by the American Physical Society under the terms of the Creative Commons Attribution 4.0 International license. Further distribution of this work must maintain attribution to the author(s) and the published article's title, journal citation, and DOI.

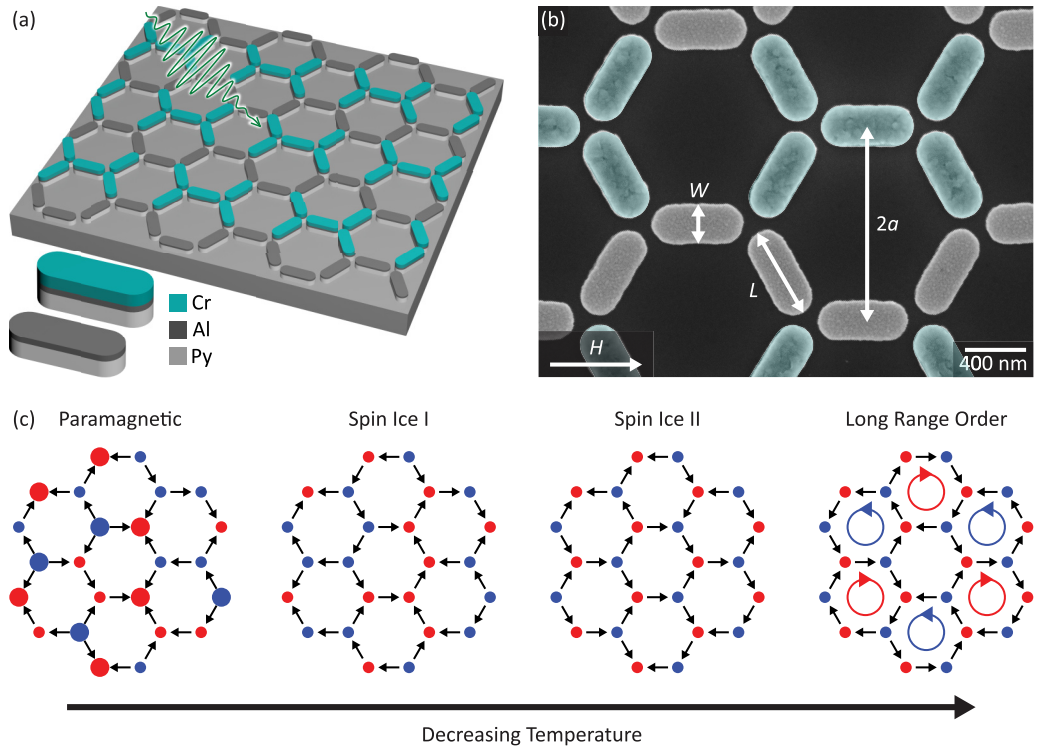


FIG. 1. Design of the kagome ASI encoded with site-selectivity and its magnetic phases. (a) Schematic of the kagome ASI consisting of Py nanomagnets fabricated on a Si substrate and capped either with Al or with Al/Cr. The Cr capping layer (shown in turquoise) has a higher optical absorption than the Al capping layer (shown in dark gray), enabling sublattice-selective laser activation while maintaining magnetic equivalence between the nanomagnet sublattices. (b) Scanning electron microscopy image of the kagome ASI, consisting of permalloy nanomagnets with length $L = 300$ nm, width $W = 100$ nm, and lattice constant $a = 320$ nm. The center-to-center distance between nanomagnets across a hexagonal plaquette is $2a$. Nanomagnets capped with an Al/Cr bilayer are highlighted in turquoise. The orientation of the applied magnetic field H is also indicated. (c) Schematics of theoretically predicted magnetic phases of kagome ice obtained on cooling. Small red (blue) dots correspond to the charges associated with ice-rule-obeying 2-in/1-out (1-in/2-out) vertex configurations, while large red (blue) dots indicate the charges associated with high-energy 3-in (3-out) defects. In the high-temperature paramagnetic regime, spins fluctuate back and forth without correlations. As the temperature is reduced, the Spin Ice I phase is reached where the ice rule is obeyed at every vertex. This is followed by the Spin Ice II phase, which exhibits long-range ordering of vertex charges, where neighboring charges alternate in sign. At the lowest temperatures, dipolar interactions stabilize the long-range ordered ground state with alternating clockwise (red arrows) and counterclockwise (blue arrows) loops of spins.

in Fig. 1(c). Here the arrows on the schematics denote the spins, small red (blue) dots correspond to ice-rule-obeying 2-in/1-out (1-in/2-out) vertex configurations, and large red (blue) dots indicate high-energy 3-in (3-out) defects. Going from left to right in Fig. 1(c), at high temperature, the system is in a paramagnetic phase. Then, on cooling, the system first enters a globally disordered but ice-rule-obeying regime known as Spin Ice I. Further cooling promotes the Spin Ice II phase, in which the vertex magnetic charges $Q = \pm q$ arrange in an alternating pattern where every positive (negative) charge is surrounded by three negative (positive) charges. Experimentally, signatures of charge ordering and charge-domain formation in kagome ASI have been reported in several thermally activated or athermal magnetic-field-driven implementations [19–21]. This ordered charge configuration emerges despite the disorder in the underlying spins, which are allowed to fluctuate through the reversal of closed, and therefore divergence-free, loops of spins, at least theoretically, so that the charge order is maintained. At even lower temperatures, long-range dipolar interactions select a long-range-ordered spin-crystal ground state characterized by alternating clockwise-counterclockwise loops of head-to-tail spins on the hexagonal plaquettes surrounding a plaquette with head-to-head/tail-to-tail spins.

While this sequence of phases is well established theoretically, in experimental systems the magnetization dynamics can become arrested before the ground state is reached. This behavior is commonly referred to as dynamical freezing, a collective effect in which the system becomes kinetically trapped in a metastable state before attaining equilibrium [22]. In practice, such freezing often occurs at temperatures above those required to access the Spin Ice II (charge-ordered) phase. A contributing factor is the blocking temperature, which marks the onset of thermally activated switching of individual nanomagnets on the experimental timescale. When the blocking temperature exceeds the critical temperature associated with collective ordering, thermal activation ceases before the system can fully explore the low-energy configurations. We emphasize, however, that a reduced blocking temperature is a necessary but not sufficient condition to reach the ground state, since quenched disorder and kinetic constraints can still prevent ordering even in thermally active

regimes. Indeed, experimental strategies based on including materials that give thermally active nanomagnets close to room temperature and thermal annealing protocols have been explored [20,23,24], yet reproducible access to the kagome ice ground state remains a challenge.

While indirect characterization methods have provided evidence of low-temperature phase transitions in kagome ASI [5], the corresponding ordered phases have never been observed [6,21]. This has motivated the search for alternative innovative strategies such as exploiting the interfacial Dzyaloshinskii-Moriya interaction (DMI), which reduces the energy barrier to nanomagnet switching. However, this method has only brought a partial charge ordering in kagome ASIs that are disconnected, i.e., made up of arrays of separated nanomagnets [25]. Therefore, up to now, accessing the ground state has typically required breaking the local symmetry of the lattice. In particular, by introducing an asymmetry in the design of the vertices, the degeneracy of vertex configurations can be lifted and the ground state stabilized. In connected ASIs formed from nanowire networks, this has been achieved through nanoscale notches [22] or asymmetric magnetic bridges [26], enabling direct imaging of the magnetic configurations during the phase transitions that lead to the lowest-energy state. In addition, Yue *et al.* [27] demonstrated that ground-state crystallization can be achieved in fully disconnected ASIs by modifying the lengths of specific nanomagnets. However, while effective, this strategy also relies on geometric modifications to the lattice, thus altering the intrinsic frustration.

Alternative methods to achieve the ground state in kagome ASI are based on local manipulation of the magnetization. For example, magnetic force microscopy (MFM) tips have been successfully used to define specific microstates, including the kagome ASI ground state [28]. However, this method is inherently serial and therefore has a low throughput, making it unsuitable for writing magnetic configurations into large arrays of nanomagnets. Recent advances in exchange bias patterning offer a partial solution to this scalability issue by spatially modulating the local coercivity in ASIs to allow selective reversal of subsets of macrospins with a global magnetic field [29]. It is also possible to tailor the width, and thus the shape anisotropy, of selected nanomagnets to deterministically set their switching thresholds (see, for example, Ref. [30] and the supplementary information associated with Ref. [4]). This can be, for example, used to set the chirality of loops of macrospins in the hexagonal plaquettes of kagome ASI [31]. However, while effective, this approach also relies on introducing an asymmetry in the geometry and therefore alters the intrinsic frustration of the lattice. These limitations highlight the need for an approach that can address large arrays, while preserving the intrinsic frustration and ensuring rapid and reliable stabilization of specific states in kagome ASIs, particularly the ground state.

Here we present a deterministic method for accessing the spin-crystal ground state of kagome ASI via ultrafast, site-selective laser-induced magnetic ordering. To this end, we fabricate a kagome ASI composed of disconnected permalloy nanomagnets arranged into two interleaved sublattices as shown in Figs. 1(a) and 1(b). While both nanomagnet sublattices are identical in terms of their magnetic properties, they are differentiated by their capping layers: One is capped with Al (in dark gray), while the other is capped with an Al/Cr bilayer (in turquoise). As a result of the optical attenuation by Cr, on illumination of the kagome ASI with an ultrafast laser pulse, the underlying magnetic elements capped with Al/Cr receive significantly less laser energy than those capped only with Al. This enables precise control of the delivery of energy at the sublattice level to attain the ground state without introducing any geometrical asymmetry in the kagome ASI.

By carefully selecting the fluence associated with the ultrafast laser exposure, the nanomagnet sublattice with the Al cap—so without a Cr layer—absorbs sufficient energy to undergo almost complete ultrafast laser-induced demagnetization, as seen in permalloy thin films and other nanomagnet ensembles [32–34]. These thermally activated nanomagnets can then relax and reverse their magnetization under an applied magnetic field, while the elements capped with Al/Cr remain magnetically frozen. The resulting macrospin configuration corresponds to the spin-crystal ground state of the kagome ASI, which we confirm by directly imaging the magnetic configurations with MFM.

We thus demonstrate deterministic and ultrafast access to the kagome ASI ground state over large areas, in a fully disconnected ASI, without relying on structural or material-induced changes to the magnetic properties. This establishes a route to rapidly control the magnetic configurations in ASIs through sublattice-selective laser excitation, without altering the intrinsic magnetic frustration.

II. SAMPLE PREPARATION AND EXPERIMENTAL SETUP

To experimentally demonstrate this concept, we fabricated kagome ASIs specifically designed to host these two optically distinguishable yet magnetically equivalent sublattices. The kagome ASIs consisted of 100×100 μm^2 arrays of 8-nm-thick permalloy (Py; $Ni_{83}Fe_{17}$) nanomagnets, which included approximately 84 570 nanomagnets. The nanomagnet arrays were patterned on silicon (100) substrates using electron beam lithography in combination with thermal evaporation of permalloy at a base pressure of 6×10^{-6} mbar and lift-off. The nanomagnets had a nominal length and width of $L = 300$ nm and $W = 100$ nm, and a lattice constant of $a = 320$ nm, as illustrated in the scanning electron microscopy image of part of a kagome ASI in Fig. 1(b). The nanomagnets were initially capped with a 3-nm-thick aluminum layer to prevent oxidation. To create differential optical absorption on the different nanomagnet sublattices while preserving magnetic equivalence, in a second lithography step, an additional 6-nm-thick Cr layer was deposited on one sublattice, resulting in interleaved Py/Al and Py/Al/Cr nanomagnets, as depicted in Fig. 1(a) and further discussed in Sec. IV A. This choice of layer stacks for the two nanomagnet sublattices, with the magnetic layer being deposited within the same lithography step, ensured that the only difference between sublattices is in their optical response. The coercive field of the kagome ASI was measured with magneto-optic Kerr effect microscopy to be ∼200 Oe.

As an alternative implementation, in a separate set of samples, we also realized kagome ASIs in which both nanomagnet sublattices consisted of Py/Al nanomagnets but with

different Py thicknesses (8 and 14 nm) defined in two successive lithography steps. This alternative approach is discussed in Sec. IV C.

Ultrafast annealing was performed with a femtosecond ytterbium-doped fiber pulsed laser (1030-nm fundamental wavelength, 200-kHz repetition rate), frequency-doubled to a wavelength of 515 nm using a barium borate (BBO) crystal and applied at an incident angle of 45 °. The laser pulses had a duration of ∼100 fs and a focal spot size on the sample of ∼85 μm full width at half maximum (FWHM).

Two laser annealing protocols were employed in this work. In Sec. III, a decreasing-fluence protocol was used, in which the sample was exposed to a sequence of laser pulses with gradually decreasing fluence in order to promote collective magnetic relaxation in a uniform kagome ASI. In Sec. IV, a constant-fluence protocol was employed to achieve deterministic, sublattice-selective switching under an applied subcoercive magnetic field.

For the constant-fluence protocol, an average power of 45 mW, which corresponded to a laser fluence of 7.9 mJ/cm^2, was applied to give an almost complete demagnetization of the Al-capped nanomagnets, thus allowing their reversal in a subcoercive field, while the Al/Cr-capped elements remained below the reversal threshold (Sec. IV A). The same constant-fluence protocol was employed for the thickness-varying sample, where sublattice selectivity instead arises from the different thermal responses of nanomagnets with different Py thicknesses (Sec. IV C).

The resulting magnetic configurations were imaged *ex situ* using MFM. The spin maps were reconstructed from the MFM images by analyzing the magnetic contrast. Here the two ends of each nanomagnet appear bright and dark, which corresponds to stray field at the north and south pole, respectively. For this, using a Python script, the position of each nanomagnet was identified from the corresponding topographic image, and the magnetization direction was assigned by evaluating the gradient in contrast along the nanomagnet long axis.

III. ULTRAFAST LASER-INDUCED MAGNETIC ORDERING IN UNIFORM KAGOME ASI

Before introducing sublattice selectivity, we first tested whether ultrafast laser annealing alone could drive the kagome ASI towards low-energy magnetic configurations. For this, we implemented the same decreasing-fluence protocol that we previously developed for square ASI [34]. This protocol involves exposing the sample to a sequence of femtosecond laser pulses at gradually decreasing fluence, going from 9.7 down to 6.1 mJ/cm^2 in steps of 13.2 nJ/cm^2, over a 1-s total exposure duration. At high fluence, ultrafast demagnetization and thermal fluctuations are sufficient to activate magnetization reversal in all nanomagnets. We can assume that there is a distribution in the energy barriers to switching of the nanomagnets [4], which is a result of the variability in the nanomagnet shape and microstructure as well as differences in the local magnetic fields. Inherent quenched disorder is known to strongly influence both relaxation pathways and the ability to reach low-energy states under magnetic-field-based driving protocols [4,35–37]. As the laser fluence gradually decreases, it seems likely that nanomagnets with higher energy barriers freeze first, while those with lower energy barriers continue to switch. The frozen magnets can form local nucleation centers that seed the growth of ordered magnetic domains. Dipolar interactions between already-frozen and still-active nanomagnets therefore guide the relaxation process, promoting the formation of low-energy configurations as the system cools down. In square ASI, this mechanism enables collective relaxation into well-ordered magnetic states [34], achieving a level of order at ultrafast timescales that is comparable or superior to that obtained via conventional thermal annealing [38–40] but without the need for prolonged equilibration protocols. In the current work, the goal is to evaluate whether such a decreasing-fluence protocol using an ultrafast laser could also be effective in achieving the ground state for the more frustrated geometry of the kagome ASI.

Following laser annealing, an 8×8 μm^2 region of the uniform kagome ASI, including ∼540 nanomagnets, was imaged using MFM as shown in Fig. 2(a). The size of this region was chosen to ensure that all of the nanomagnets were exposed to a laser fluence that is sufficiently high to demagnetize them and therefore allow them to switch. The macrospin orientations were reconstructed from the magnetic contrast in the 8×8 μm^2 area, yielding the magnetic configuration shown in Fig. 2(b). From this reconstructed configuration, we determined the charge-charge correlators [18,21,41], which give an indication of the degree of magnetic ordering. While the spin-spin correlators also give insight into the magnetic ordering, the charge-charge correlators give an immediate quantitative signature of how far the system has entered the Spin Ice II phase. The charge-charge correlator is given by $C_{ij} = \langle Q_i Q_j \rangle / q^2$, which quantifies the degree of correlation between the signs of charges Q_i and Q_j. Defining the location of the charges at representative vertices A, B, and C shown in Fig. 2(a), we determine the magnitude of C_{ij} in the 8×8 μm^2 region for the first nearest neighbors, C_{AB}, and second nearest neighbors C_{AC}. In the ideal Spin Ice II phase, first nearest neighbors are perfectly anticorrelated ($C_{AB} = -1$) and second neighbors are perfectly correlated ($C_{AC} = +1$). For our laser annealed experimental systems, we find that $C_{AB} \sim -0.3$, indicating partial charge ordering, while $C_{AC} \sim +0.1$, consistent with a weak tendency towards the expected charge correlation of the Spin Ice II phase. These charge-charge correlators indicate the formation of vertex charge patterns consistent with partial charge crystallization [19–21], with the charge-ordered crystallites highlighted with gray shading in Fig. 2(b), and are comparable to those reported for DMI-assisted thermal annealing in disconnected kagome ASIs [25]. Crucially, our femtosecond laser annealing achieves a comparable degree of ordering without altering the intrinsic magnetic properties of the system with geometrical or material modifications, and at a much shorter timescale.

We emphasize that the purpose of the work outlined in this section is to benchmark the effectiveness of ultrafast laser annealing in uniform kagome ASI and to motivate the site-selective strategy presented below. The decreasing-fluence protocol was adopted from Ref. [34] and selected based on optimization trials where this protocol was found to consistently yield the highest degree of magnetic ordering among the conditions explored. The pulse duration (100 fs) is fixed by the

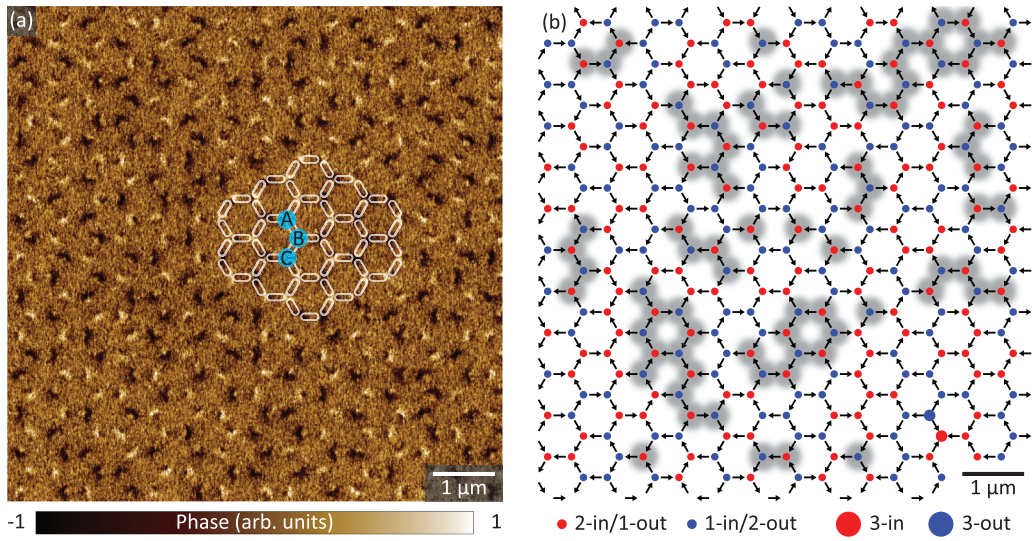


FIG. 2. Magnetic configuration of the uniform kagome ASI after ultrafast laser annealing revealed by MFM imaging and reconstructed spin map, together with the vertex charges. (a) MFM image of the uniform kagome ASI following ultrafast laser annealing. Bright (dark) contrast corresponds to the magnetic stray field associated with the north (south) magnetic poles at the ends of the nanomagnets. The location of the nanomagnets in part of the image is indicated with white borders and three representative vertices are highlighted (A, B and C), illustrating how nearest-neighbor (A-B) and next-nearest-neighbor (A-C) charge correlators are defined. (b) Reconstructed spin and vertex charge map obtained from the MFM image in (a), where small red (blue) dots correspond to the $+q\,(-q)$ charges associated with 2-in/1-out (1-in/2-out) ice-rule-obeying vertices, and large red (blue) dots indicate the $+3q\,(-3q)$ charges associated with high-energy 3-in (3-out) defects. Unit vertex charges surrounded by three unit charges of opposite sign are highlighted with gray shading revealing partial charge crystallization consistent with the onset of the Spin Ice II phase.

laser system and was not varied. The repetition rate was kept at 200 kHz and, as demonstrated in our previous work [34], the sample fully relaxes back to room temperature between successive pulses, such that no cumulative heating occurs and each laser pulse acts independently.

It should also be mentioned that traditional approaches to access low-energy states in ASI have relied on demagnetization in a global magnetic field, either applying an alternating magnetic field or rotating the sample in a static magnetic field. This can yield partial ordering but, typically, the resulting magnetic configurations are sensitive to quenched disorder and are not inherently deterministic [42–44]. For the annealing experiments on the uniform kagome ASI reported in this section, no external magnetic field was applied.

IV. DETERMINISTIC GROUND STATE WRITING VIA SUBLATTICE-SELECTIVE LASER ANNEALING

While we have shown that laser annealing can promote charge ordering to a certain extent in kagome ASI, accessing the long-range ordered spin-crystal ground state requires a more targeted strategy. We exploit the fact that, in the ground state, when the magnetic moments of the nanomagnets are projected onto a fixed in-plane axis, in this case the x axis (see coordinate axes in Fig. 3), the lattice decomposes into two interleaved sublattices (distinguished by macrospins outlined and not outlined in black in Fig. 3) with macrospin components that point in opposite directions [see Fig. 3(d)]. Starting from a magnetic configuration with all macrospins pointing towards $+x$ [see Fig. 3(a)], reversing the macrospins of only one of the two nanomagnet sublattices [macrospins shown in blue without an outline in Fig. 3(d)], yields the spin-crystal ground state in a single step. This insight motivates our experimental design: We selectively address one nanomagnet sublattice under a reversed subcoercive magnetic field (i.e., the sublattice containing macrospins without a black outline) while the complementary nanomagnet sublattice (containing macrospins with a black outline) remains pinned.

A. Sublattice selectivity with Cr capping

To experimentally realize the site-selective switching using magnetically and geometrically equivalent nanomagnets, we introduced a differential optical absorption between the two nanomagnet sublattices via selective Cr capping. Specifically, one nanomagnet sublattice was fabricated with a standard Py(8 nm)/Al(3 nm) stack, while the other was modified by adding a 6-nm-thick Cr capping layer above the Al layer, to give a Py(8 nm)/Al(3 nm)/Cr(6 nm) stack [Fig. 1(a)]. This configuration preserves the magnetic equivalence of the two sublattices, thus leaving the magnetic frustration unaltered. A potential concern when placing Cr in close proximity to Py is the possible presence of an exchange bias, which could affect the switching behavior. For this reason, the 3-nm-thick Al spacer was intentionally retained to prevent any direct magnetic coupling between Cr and Py. Indeed, in previous work, it has been shown that exchange bias across a ferromagnet-antiferromagnet interface decays rapidly with increasing thickness of a nonmagnetic interlayer, becoming negligible once the spacer exceeds a thickness of 1-2 nm [45]. To verify this, we measured the hysteresis loops of the Al/Cr-capped and Al-capped ASIs and found no evidence of shifted hysteresis loops or increased coercivity that is normally associated with exchange bias, thus confirming that exchange

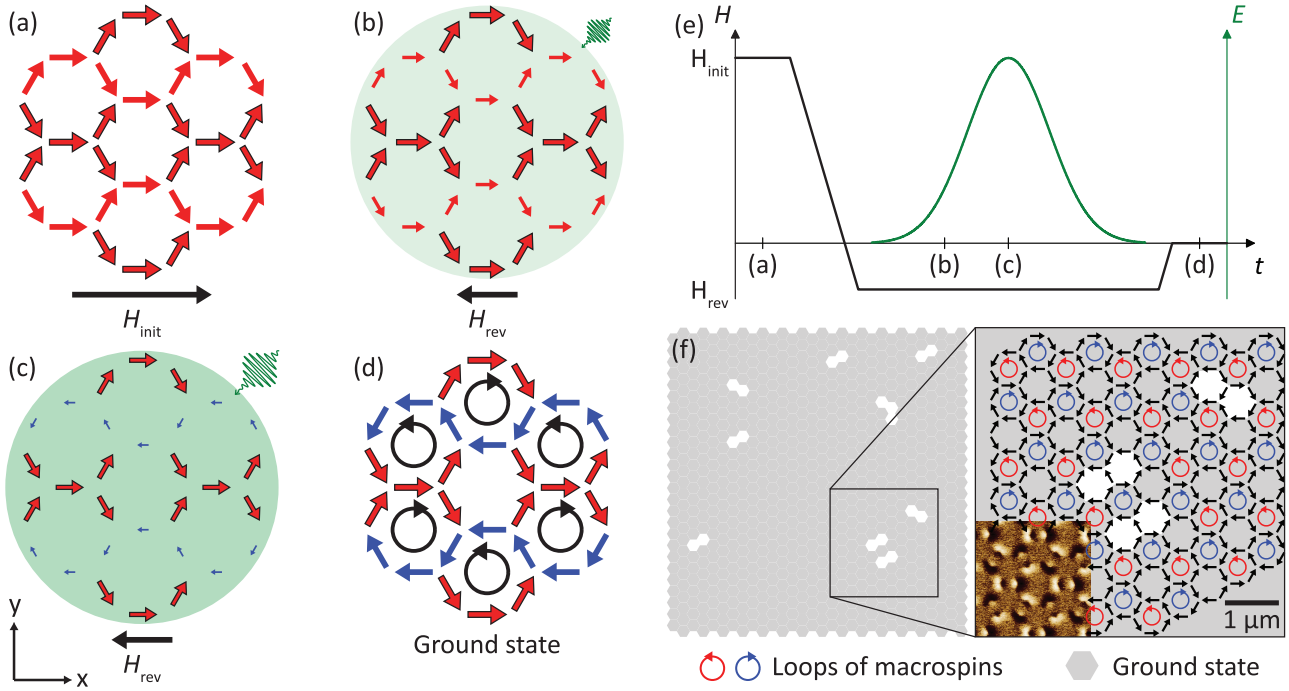


FIG. 3. Schematic representation and experimental realization of deterministic ground-state writing in kagome ASI via sublattice-selective ultrafast laser annealing. (a) The system is first initialized by applying a saturating magnetic field $H_{\text{init}} = 500$ Oe along the x direction so that, on removal of the magnetic field, all macrospins point towards the right. Macrospins outlined in black correspond to the Al/Cr-capped nanomagnet sublattice, while Al-capped elements form the complementary nanomagnet sublattice with macrospins not outlined in black. (b) A reverse magnetic field of $H_{\text{rev}} = 50$ Oe is then applied, which is well below the ∼200 Oe coercive field of the nanomagnets, and the laser exposure (indicated with a circular region shaded in green) begins to demagnetize the nanomagnets. (c) At a later time during laser exposure, the Al-capped nanomagnets absorb sufficient energy to become sufficiently demagnetized so that they switch their residual magnetization under the reverse magnetic field, while the magnetization in the Al/Cr-capped elements remains large enough to prevent reversal. (d) After the laser pulse terminates, the system's magnetization recovers giving the fully ordered spin-crystal ground state, maximizing the number of alternating clockwise and counterclockwise loops of macrospins. (e) Schematic representation of the experimental protocol indicating how the applied magnetic field H and the laser pulse energy E change over time t. The labels (a) to (d) indicate the different stages in the corresponding figure panels. While this schematic shows the anticipated process for a single laser pulse, in the experiment we employ a train of pulses to ensure a stable laser output. The time axis is also not to scale: The magnetic field is applied quasistatically (over seconds), while the laser excitation consists of ultrashort pulses (∼100 fs) delivered as a pulse train during the exposure for which only a single pulse is shown here. (f) Macrospin configuration obtained with MFM over a 20×20 μm^2 region, which is well within the laser spot that has a size of ∼85 μm (FWHM). This confirms the formation of long-range order (hexagonal plaquettes shown in gray) with only a few defects, i.e., deviations from the ground state (hexagonal plaquettes shown in white), which are likely to be due to local fabrication irregularities. A fully ordered region of the original MFM image has been included to illustrate the correspondence between the measured contrast and the reconstructed configuration.

bias is not present within the limits set by the instrumental accuracy.

We now apply an experimental protocol to deterministically achieve the ground state, which involves varying the magnetic field in time and exploiting the intrinsic temporal profile of the pulsed laser. A simplified schematic of the applied protocol, considering a single laser pulse, is shown in Fig. 3(e). Before laser exposure, the entire system was initialized in a uniform magnetic state by applying a saturating magnetic field $H_{\text{init}} = 500$ Oe along the x direction [Fig. 3(a)]. After removing the magnetic field, the magnetic moments of all nanomagnets remained aligned towards x, as illustrated in Fig. 3(a). A reverse magnetic field $H_{\text{rev}} = -50$ Oe, well below the ∼200 Oe coercive field of the kagome ASI, was then applied and maintained during the laser annealing process [Figs. 3(b) and 3(c)]. While only a single laser pulse is shown in the simplified schematic in Fig. 3(e), for the laser annealing experiment, the ASI was exposed to a train of femtosecond laser pulses at a constant fluence of 7.9 mJ/cm^2 for 1 s. We envisage that the reversal of the nanomagnet sublattice without the Cr layer proceeded as follows. At first, the magnetic moments of all nanomagnets still pointed towards x [Fig. 3(b)], since they were not sufficiently demagnetized to reverse under the applied subcoercive field. Subsequently, only the Al-capped nanomagnets absorbed sufficient energy to reach thermal activation [Fig. 3(c)], enabling magnetization reversal of the macrospins without the black outline in Figs. 3(a)–3(d) under the reversed subcoercive field, while the magnetic moments in the Al/Cr-capped elements [with a black outline in Figs. 3(a)–3(d)], maintained their original orientation. After the laser pulse was terminated and the applied magnetic field was removed [Fig. 3(d)], MFM imaging revealed that the scanned region (∼ 20×20 μm^2), which is well within the laser spot size of ∼85 μm (FWHM), relaxed into a nearly perfect spin-crystal ground state. The reconstructed spin map, obtained from the analysis of the MFM

magnetic contrast, is shown in Fig. 3(f), where ground-state hexagonal plaquettes are highlighted in gray. White regions indicate defects where the hexagonal plaquettes are not in the ground-state configuration. These defects can be attributed to isolated fabrication errors such as shape irregularities or edge roughness that locally increase the energy barrier to switching. Since the defects normally involve the wrong orientation of a single macrospin, which is shared by two hexagonal plaquettes, the hexagonal plaquette defects shown in white usually come in pairs. A zoomed-in region in Fig. 3(f) displays the detailed magnetic configuration, which is overlaid in one corner with the corresponding MFM image, illustrating the correspondence between the measured contrast and the reconstructed spin map.

B. Simulations of laser-induced heat transfer in uncapped and Cr-capped stacks

To further support the experimental findings, we performed simulations of laser-induced heat transfer in Py/Al and Py/Al/Cr stacks. The simulations were carried out using the "Heat Transfer in Solids" module in COMSOL Multiphysics with a time-dependent study and femtosecond time resolution. The incident laser beam was modeled as a Gaussian spot, with a FWHM of 85 μm as in the experiment, and with the individual pulses having a rectangular temporal profile of 100-fs duration, corresponding to the experimental laser fluence and repetition rate. The simulated geometry consisted of an 8-nm-thick Py film on a Si substrate, with and without a 6-nm-thick Cr capping layer. The Al layers were taken into account through effective interface boundary conditions but were not explicitly included as separate layers for computational efficiency. For this reason, they are denoted in parentheses for the Py/(Al) and Py/(Al)/Cr stacks when discussing the simulations. Since the laser penetration depth within the simulated time window is only ∼0.6 μm, which is much smaller than the actual substrate thickness, the Si substrate could be truncated to a thickness of 2 μm with its lower boundary maintained at ambient temperature. Heat exchange with the environment was included only through radiation from the topmost surface. The Py/(Al)/Cr and Si/Py interfaces were modeled by introducing effective thermal boundary conductances in order to account for imperfect heat transmission across material discontinuities. Further details concerning the simulations are given in Appendix A.

The absorption of the laser beam inside the exposed material was implemented following the Beer-Lambert law, which is commonly used to model laser energy deposition in thin-film heat-transfer simulations [46,47], to give an exponential attenuation of the optical intensity with depth. All simulations were initialized at an ambient temperature of 300 K. From the simulations [Fig. 4(a)], we see that, for the Py/(Al) stack, much of the optical energy is directly deposited in the magnetic (Py) layer, resulting in a sharp temperature rise across its thickness. In contrast, in the Py/(Al)/Cr stack, we see that a large fraction of the incident energy is blocked by the Cr capping layer, both because of enhanced optical reflectivity at the Cr surface and because of its large intrinsic absorption coefficient at a laser wavelength of 515 nm. As a result, the

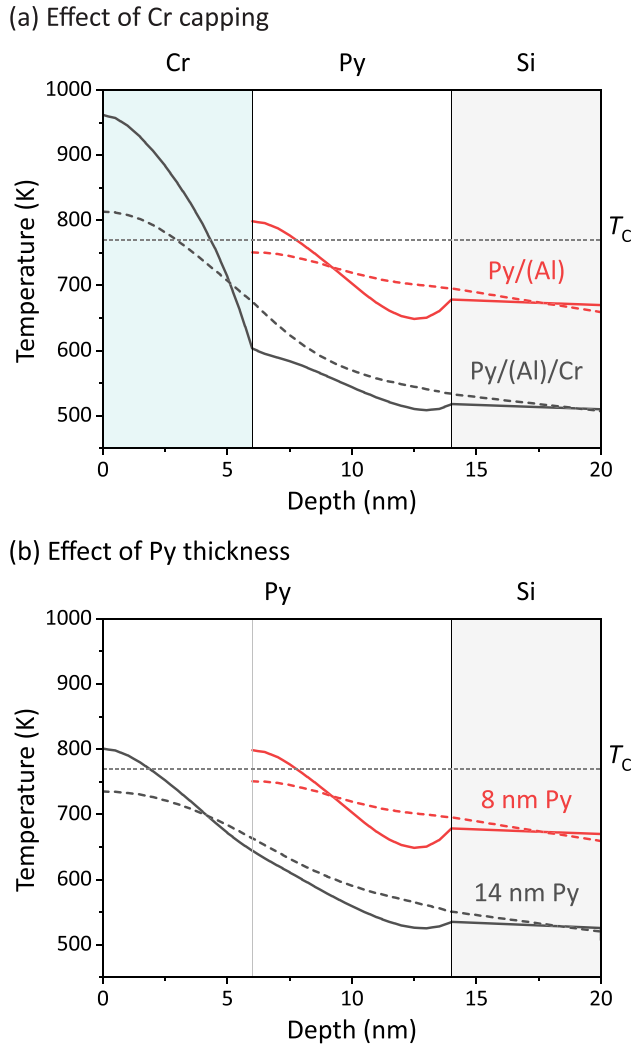


FIG. 4. Simulated temperature-depth profiles of Py/Al/Cr and Py/Al film stacks under femtosecond laser excitation. (a) Depth-resolved temperature distribution for Py nanomagnets with (black curves) and without (red curves) a Cr capping layer at two different times after the laser pulse: $t_1 = 100$ fs (solid lines) and $t_2 = 600$ fs (dashed lines). In the Cr-capped stack, most of the incident energy is absorbed in the Cr layer, where peak temperature exceeds 900 K at t_1, while the underlying Py reaches a reduced peak temperature of about 675 K at the later time t_2, and remains well below the Curie temperature $T_C \sim 770$ K. In contrast, in the Py/(Al) stack, the energy is directly deposited in the magnetic layer, which rapidly approaches T_C, enabling substantial demagnetization. Brackets for the Al layers indicate that they are not modeled as explicit layers but are instead included via effective interface boundary conditions. (b) Depth-resolved temperature distribution for different thicknesses of Py [8 nm (red curves) and 14 nm (black curves)] at two different times after the laser pulse: $t_1 = 100$ fs (solid lines) and $t_2 = 600$ fs (dashed lines). In both cases, the temperature profiles decrease with depth. The thinner magnetic layer reaches temperatures close to T_C across the thickness, whereas, in the thicker layer, only the upper region is significantly heated, leaving a large fraction of the magnetic layer well below T_C. This difference in thermal response supports the experimental results where the thinner nanomagnets undergo switching, while the thicker nanomagnets remain in their initial state during laser excitation. In both panels, the nonuniform temperature gradient can be attributed to heat reflection at the interface.

heating of the Py underneath is significantly reduced and temporally delayed.

The simulated depth-resolved temperature profiles through the stack, from the central pixel (lateral dimensions 5×5 nm^2) of the Gaussian laser spot, are shown in Fig. 4(a) for two different time delays. At $t_1 = 100$ fs, the temperature of the Cr capping layer in the Py/(Al)/Cr stack reaches a maximum of ∼960 K (black solid line), while the temperature of the Py layer in the Py/(Al) stack attains a peak value of ∼800 K (red solid line). The strong absorption of the laser light in Cr confines the energy near the surface, whereas in the Py/(Al) stack the laser energy is deposited directly within the magnetic layer and spread over its full thickness, leading to a more uniform temperature profile but a reduced peak temperature compared to the Cr-capped case. The temperature of the Py in the Py/(Al)/Cr stack reaches a maximum of ~ 675 K at $t_2 = 600$ fs (black dashed curve), which is delayed with respect to the Py/(Al) stack because heat must first diffuse through the Cr capping layer. For completeness, the temperature profile of the Py/(Al) stack at $t_2 = 600$ fs is also shown (red dashed curve), although its maximum already occurred earlier.

Overall, the simulations demonstrate that the Cr capping layer does not simply act as a passive heat shield but modifies both the spatial and temporal energy absorption profile. We can deduce that, since the temperature of the Py in the Py/(Al)/Cr stack never exceeds the Curie temperature ($T_C \sim 770$ K [40]), the Py/Al/Cr nanomagnets retain a sufficient residual magnetization to prevent reversal under the applied subcoercive magnetic field. In contrast, the simulations indicate that the Py/Al nanomagnets approach the Curie temperature, which will lead to a substantial demagnetization, thus reducing the energy barrier to switching and enabling laser-assisted magnetization reversal. These simulation results therefore provide quantitative support for the mechanism underlying the deterministic writing of kagome ASI ground states, a method that is both robust and applicable to large areas, which is essential for programmable nanomagnetic architectures.

C. Sublattice selectivity through modification of the nanomagnet thickness

Returning to the experiment, an alternative approach to optical attenuation with Cr capping for achieving sublattice selectivity is to modify the thickness of the magnetic material itself. In this implementation, one sublattice consists of standard Py/Al nanomagnets with a Py thickness of 8 nm, as before, while the other nanomagnet sublattice is fabricated with an increased Py thickness of 14 nm. All other geometrical parameters remain identical.

The laser annealing was performed using the same constant fluence pulse-train protocol described in Sec. IV A, i.e., by exposing the ASI to a train of femtosecond laser pulses at a fluence of 7.9 mJ/cm² for 1 s.

COMSOL simulations of the temperature profiles [Fig. 4(b)], under the same laser fluence used in the Cr-capping approach, reveal that the internal temperature gradient is similar for both thicknesses. Nevertheless, due to the increased thickness, much of the thicker Py layer remains far below the Curie temperature throughout the pulse duration. As a result, a substantial portion of the volume retains a significant residual magnetization that keeps the energy barrier to switching high enough so that the magnetization effectively remains frozen. In contrast, the thinner nanomagnets, with the temperature much closer to the Curie temperature, are almost entirely demagnetized, thus allowing laser-assisted reversal.

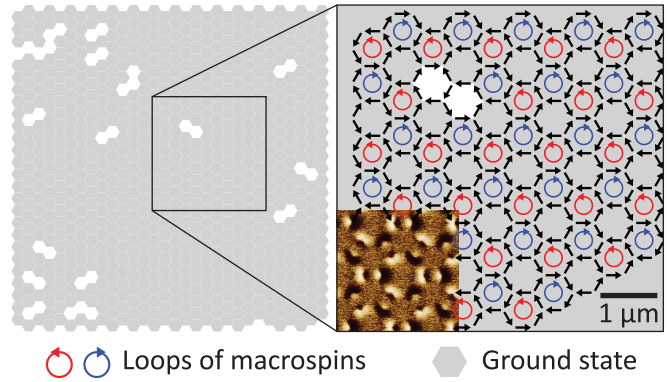


FIG. 5. Macrospin configuration of kagome ASI obtained via sublattice-selective ultrafast laser annealing based on different Py thicknesses in the two nanomagnet sublattices (8 and 14 nm). The macrospin configuration is reconstructed from the original image obtained with MFM over a 20×20 μm^2 region, which is well within the laser spot, which has a size of ∼85 μm (FWHM). Similarly to the magnetic configuration obtained using the Al/Cr capping approach shown in Fig. 3(f), the reconstruction confirms the presence of long-range order (shown in gray), characteristic of the spin-crystal ground state, with only a few defects (shown in white), which are most likely due to local fabrication irregularities. A fully ordered region of the original MFM image is included to illustrate the correspondence between the measured contrast and the reconstructed macrospin configuration.

Experimentally, on applying the same laser fluence protocol as that used in Sec. IV A, the final magnetic configuration obtained using this variable thickness approach again closely resembles the spin-crystal ground state, with long-range-ordered loops of macrospins visible across the scanned region (see Fig. 5).

Although this method does not preserve the magnetic equivalence of the two sublattices, and therefore lifts the intrinsic degeneracy of the kagome ASI, the use of thickness as a selection parameter offers the practical advantage of eliminating the need for additional capping materials. This strategy thus represents a viable and pragmatic alternative for implementations where robust and scalable optical site-selective switching is desired, while magnetic frustration is not a strict requirement. In this respect, this approach is interesting for the implementation of functional architectures, such as logic devices or reconfigurable magnetic systems.

V. CONCLUSIONS

We have demonstrated a deterministic and rewritable approach to access the spin-crystal ground state of kagome ASI

using ultrafast site-selective laser annealing. By tuning specific nanomagnet sublattices of the kagome ASI with targeted differences in optical absorption, we have enabled magnetization reversal of selected nanomagnets under subcoercive magnetic fields. The modification of the local absorption is achieved through either Cr capping or changing the nanomagnet thickness, which is realized with standard lithography methods.

Our implementation based on capping specific subsets of nanomagnets with Cr, preserves the magnetic equivalence of the nanomagnets and maintains the intrinsic frustration. Using this approach, it was possible to access the degenerate ground-state manifold, as confirmed by MFM imaging, while heat-transfer simulations supported the underlying sublattice-selective excitation mechanism. The alternative implementation, relying on thickness-based selectivity, offers a route to deterministic switching that only requires adjusting the nanomagnet thickness, so avoiding additional capping layers. Although this second method lifts the degeneracy of the low-energy states because the two nanomagnet sublattices now have different magnetic properties, it is suitable for applications where maintaining the intrinsic frustration is not critical. Both approaches provided almost perfect long-range ordered magnetic states comparable to those obtained on modifying the Kagome ASI geometry.

In summary, we have established ultrafast laser annealing as a versatile tool for controlling frustrated nanomagnetic systems over large areas, without introducing changes to the lattice geometry. Indeed, while our current experiments are restricted to the size of the laser spot, the area of exposure can be easily increased by scanning the sample under the laser beam.

The kagome ASI represents an archetypal frustrated system, whose theoretically predicted ordered ground state has been experimentally elusive due to kinetic constraints and dynamical freezing. Achieving this ground state in a controlled manner as demonstrated here is therefore an important step towards investigating fundamental phenomena such as charge crystallization, excitations above an ordered background, and controlled deviations from equilibrium in artificial frustrated systems. For this, our ultrafast site-selective laser annealing not only provides a method to reach low-energy configurations, but can do this both deterministically and reproducibly.

Beyond the specific realization of the kagome ASI ground state, the site-selective ultrafast laser annealing strategy introduced here provides a general route to locally engineer the excitation and relaxation of other ASIs. This approach enables deterministic access to selected low-energy states in ASIs consisting of arrays of identical nanomagnets, which is difficult or impossible to achieve using uniform thermal annealing or globally applied magnetic fields. As such, this strategy opens new possibilities for studying controlled excitations above ordered states, testing theoretical models of frustrated magnetism, and extending the deterministic preparation of specific magnetic states to other ASI geometries.

Finally, this method offers new opportunities for constructing input-selective nanomagnetic logic circuits and neuromorphic computing architectures, where different nanomagnets can be addressed at specific laser fluences. This approach also provides a route to design reprogrammable magnonic crystals with the ability to encode specific magnetic states, and to reset and re-established the magnetic configuration, using the same laser excitation protocol. This provides a means to precisely tune the spin-wave spectra during device operation at ultrafast timescales.

ACKNOWLEDGMENTS

The authors acknowledge financial support from the Swiss National Science Foundation (Grant No. 200020_200332). We thank Gavin Macauley for developing the Python code used for the macrospin reconstruction analysis, Anja Weber and the PICO cleanroom staff at the Paul Scherrer Institute for technical support during the nanofabrication process, the members of the Mesoscopic Systems group for their assistance in the laboratory, and the Scanning Probe Microscopy Laboratory at the Paul Scherrer Institute for supporting the MFM measurements.

DATA AVAILABILITY

The data that support the findings of this article are openly available [48].

APPENDIX: FURTHER DETAILS CONCERNING THE LASER-INDUCED HEAT TRANSFER SIMULATIONS

The laser-induced heating was simulated by solving the time-dependent heat-diffusion equation,

$$\rho C_p \frac{\partial T}{\partial t} = \nabla \cdot (k \nabla T) + Q(\mathbf{r}, t),$$

where T is the temperature, k the thermal conductivity, ρ the mass density, and C_p the specific heat capacity of each material. The simulations were performed within a single-temperature framework using the "Heat Transfer in Solids" module of COMSOL Multiphysics, such that the computed temperature corresponds to the lattice temperature. Temperature-dependent material parameters for Py, Cr, and Si were taken from the COMSOL materials library. All material parameters used in the simulations (thermal conductivity, density, and specific heat) correspond to standard literature values and are provided in the COMSOL materials database.

Laser excitation was implemented as a volumetric heat source $Q(\mathbf{r}, t)$ with a Gaussian spatial profile matching the experimental spot size (85 μm FWHM) and a rectangular temporal profile with a duration of 100 fs. Optical absorption in the metallic layers was modeled using Beer-Lambert attenuation, such that the deposited energy decays exponentially with depth. The total energy deposited per pulse was determined by the experimentally applied laser fluence, which sets the amplitude of the volumetric heat source in the simulations. The Al spacer layer was not explicitly discretized but was accounted for by implementing effective thermal boundary conductances at the interfaces.

The simulated geometry consisted of Py films (with or without a Cr capping layer) on a truncated Si substrate of thickness 2 μm. The bottom surface of the substrate was held at ambient temperature, while all other external boundaries were treated as thermally insulating. Interfacial heat transfer at the Py/(Al)/Cr and Py/Si interfaces was modeled using

effective thermal boundary conductances. The model system was discretized using a nonuniform finite-element mesh, in which the element size varies across the simulation domain, with subnanometer elements in the metallic layers and progressively coarser elements in the substrate, increasing in size from a few nanometers near the interfaces up to tens of nanometers at the bottom of the truncated Si substrate. A time step of 1 fs was implemented.

The single-temperature model does not explicitly describe nonequilibrium electron dynamics during the first tens to hundreds of femtoseconds following laser excitation. However, since electron-phonon equilibration in metals occurs on the subpicosecond to few picosecond timescale, the simulated temperature represents the lattice temperature reached shortly after the pulse. This is the relevant quantity for assessing whether the permalloy layer approaches the Curie temperature and undergoes substantial demagnetization, which is the key criterion for obtaining thermally assisted magnetization reversal in the present experiments.

[1] S. H. Skjærvø, C. H. Marrows, R. L. Stamps, and L. J. Heyderman, Advances in artificial spin ice, Nat. Rev. Phys. **2**, 13 (2020).

[2] M. J. Harris, S. T. Bramwell, D. F. McMorrow, T. Zeiske, and K. W. Godfrey, Geometrical frustration in the ferromagnetic pyrochlore $Ho_2Ti_2O_7$, Phys. Rev. Lett. **79**, 2554 (1997).

[3] S. Ladak, D. E. Read, G. K. Perkins, L. F. Cohen, and W. R. Branford, Direct observation of magnetic monopole defects in an artificial spin-ice system, Nat. Phys. **6**, 359 (2010).

[4] E. Mengotti, L. J. Heyderman, A. F. Rodríguez, F. Nolting, R. V. Hügli, and H.-B. Braun, Real-space observation of emergent magnetic monopoles and associated Dirac strings in artificial kagome spin ice, Nat. Phys. **7**, 68 (2011).

[5] L. Anghinolfi, H. Luetkens, J. Perron, M. G. Flokstra, O. Sendetskyi, A. Suter, T. Prokscha, P. M. Derlet, S. L. Lee, and L. J. Heyderman, Thermodynamic phase transitions in a frustrated magnetic metamaterial, Nat. Commun. **6**, 8278 (2015).

[6] O. Sendetskyi, L. Anghinolfi, V. Scagnoli, G. Möller, N. Leo, A. Alberca, J. Kohlbrecher, J. Lüning, U. Staub, and L. J. Heyderman, Magnetic diffuse scattering in artificial kagome spin ice, Phys. Rev. B **93**, 224413 (2016).

[7] O. Sendetskyi, V. Scagnoli, N. Leo, L. Anghinolfi, A. Alberca, J. Lüning, U. Staub, P. M. Derlet, and L. J. Heyderman, Continuous magnetic phase transition in artificial square ice, Phys. Rev. B **99**, 214430 (2019).

[8] M. Goryca, X. Zhang, J. D. Watts, C. Nisoli, C. Leighton, P. Schiffer, and S. A. Crooker, Magnetic field–dependent thermodynamic properties of square and quadrupolar artificial spin ice, Phys. Rev. B **105**, 094406 (2022).

[9] R. F. Wang, C. Nisoli, R. S. Freitas, J. Li, W. McConville, B. J. Cooley, M. S. Lund, N. Samarth, C. Leighton, V. H. Crespi, and P. Schiffer, Artificial 'spin ice' in a geometrically frustrated lattice of nanoscale ferromagnetic islands, Nature (Lond.) **439**, 303 (2006).

[10] C. Nisoli, Frustration(s) and the ice rule: From natural materials to the deliberate design of exotic behaviors, in *Frustrated Materials and Ferroic Glasses*, edited by T. Lookman, and X. Ren, Vol. 275 (Springer International Publishing, Cham, 2018), pp. 57–99.

[11] E. Mengotti, L. J. Heyderman, A. Fraile Rodríguez, A. Bisig, L. Le Guyader, F. Nolting, and H. B. Braun, Building blocks of an artificial kagome spin ice: Photoemission electron microscopy of arrays of ferromagnetic islands, Phys. Rev. B **78**, 144402 (2008).

[12] M. Tanaka, E. Saitoh, H. Miyajima, T. Yamaoka, and Y. Iye, Magnetic interactions in a ferromagnetic honeycomb nanoscale network, Phys. Rev. B **73**, 052411 (2006).

[13] Y. Qi, T. Brintlinger, and J. Cumings, Direct observation of the ice rule in an artificial kagome spin ice, Phys. Rev. B **77**, 094418 (2008).

[14] G. Möller and R. Moessner, Magnetic multipole analysis of kagome and artificial spin-ice dipolar arrays, Phys. Rev. B **80**, 140409(R) (2009).

[15] G.-W. Chern, P. Mellado, and O. Tchernyshyov, Two-stage ordering of spins in dipolar spin ice on the kagome lattice, Phys. Rev. Lett. **106**, 207202 (2011).

[16] G.-W. Chern and O. Tchernyshyov, Magnetic charge and ordering in kagome spin ice, Philos. Trans. R. Soc. Math. Phys. Eng. Sci. **370**, 5718 (2012).

[17] C. Castelnovo, R. Moessner, and S. L. Sondhi, Magnetic monopoles in spin ice, Nature (Lond.) **451**, 42 (2008).

[18] A. Farhan, P. M. Derlet, L. Anghinolfi, A. Kleibert, and L. J. Heyderman, Magnetic charge and moment dynamics in artificial kagome spin ice, Phys. Rev. B **96**, 064409 (2017).

[19] N. Rougemaille, F. Montaigne, B. Canals, A. Duluard, D. Lacour, M. Hehn, R. Belkhou, O. Fruchart, S. El Moussaoui, A. Bendounan, and F. Maccherozzi, Artificial kagome arrays of nanomagnets: A frozen dipolar spin ice, Phys. Rev. Lett. **106**, 057209 (2011).

[20] F. Montaigne, D. Lacour, I. A. Chioar, N. Rougemaille, D. Louis, S. M. Murtry, H. Riahi, B. S. Burgos, T. O. Menteş, A. Locatelli, B. Canals, and M. Hehn, Size distribution of magnetic charge domains in thermally activated but out-of-equilibrium artificial spin ice, Sci. Rep. **4**, 5702 (2014).

[21] S. Zhang, I. Gilbert, C. Nisoli, G.-W. Chern, M. J. Erickson, L. O'Brien, C. Leighton, P. E. Lammert, V. H. Crespi, and P. Schiffer, Crystallites of magnetic charges in artificial spin ice, Nature (Lond.) **500**, 553 (2013).

[22] V. Schánilec, B. Canals, V. Uhlíř, L. Flajšman, J. Sadílek, T. Šikola, and N. Rougemaille, Bypassing dynamical freezing in artificial kagome ice, Phys. Rev. Lett. **125**, 057203 (2020).

[23] J. Drisko, T. Marsh, and J. Cumings, Topological frustration of artificial spin ice, Nat. Commun. **8**, 14009 (2017).

[24] J. Drisko, $FePd_3$ as a material for studying thermally active artificial spin ice systems, Phys. Rev. B **91**, 224406 (2015).

[25] K. Hofhuis, A. Hrabec, H. Arava, N. Leo, Y.-L. Huang, R. V. Chopdekar, S. Parchenko, A. Kleibert, S. Koraltan, C. Abert, C. Vogler, D. Suess, P. M. Derlet, and L. J. Heyderman, Thermally superactive artificial kagome spin ice structures obtained with

the interfacial Dzyaloshinskii-Moriya interaction, Phys. Rev. B **102**, 180405 (2020).

[26] K. Hofhuis, S. H. Skjærvø, S. Parchenko, H. Arava, Z. Luo, A. Kleibert, P. M. Derlet, and L. J. Heyderman, Real-space imaging of phase transitions in bridged artificial kagome spin ice, Nat. Phys. **18**, 699 (2022).

[27] W.-C. Yue, Z. Yuan, Y.-Y. Lyu, S. Dong, J. Zhou, Z.-L. Xiao, L. He, X. Tu, Y. Dong, H. Wang, W. Xu, L. Kang, P. Wu, C. Nisoli, W.-K. Kwok, and Y.-L. Wang, Crystallizing kagome artificial spin ice, Phys. Rev. Lett. **129**, 057202 (2022).

[28] J. Gartside, D. Arroo, D. Burn, V. Bemmer, A. Moskalenko, L. Cohen, and W. Branford, Realization of ground state in artificial kagome spin ice via topological defect-driven magnetic writing, Nat. Nanotechnol. **13**, 53 (2018).

[29] V. M. Parakkat, G. M. Macauley, R. L. Stamps, and K. M. Krishnan, Configurable artificial spin ice with site-specific local magnetic fields, Phys. Rev. Lett. **126**, 017203 (2021).

[30] R. V. Hügli, G. Duff, B. O'Conchuir, E. Mengotti, A. F. Rodríguez, F. Nolting, L. J. Heyderman, and H. B. Braun, Artificial kagome spin ice: Dimensional reduction, avalanche control and emergent magnetic monopoles, Philos. Trans. R. Soc. Math. Phys. Eng. Sci. **370**, 5767 (2012).

[31] R. V. Chopdekar, G. Duff, R. V. Hügli, E. Mengotti, D. A. Zanin, L. J. Heyderman, and H. B. Braun, Controlling vortex chirality in hexagonal building blocks of artificial spin ice, New J. Phys. **15**, 125033 (2013).

[32] S. N. Panda, S. Mondal, S. Majumder, and A. Barman, Ultrafast demagnetization and precession in permalloy films with varying thickness, Phys. Rev. B **108**, 144421 (2023).

[33] Z. Liang, T. Bu, Z. Lyu, Z. Liu, A. Hrabec, L. Wang, Y. Dou, J. Ding, P. Ge, W. Yang, T. Huang, J. Yang, L. J. Heyderman, Y. Liu, Z. Yu, and Z. Luo, Ultrafast probabilistic neuron in an artificial spin ice for robust deep neural networks, Adv. Funct. Mater. **35**, 2417334 (2025).

[34] D. Pecchio, S. Sahoo, O. Chubykalo-Fesenko, S. Koraltan, G. M. Macauley, T. Thomson, D. Suess, V. Scagnoli, and L. J. Heyderman, Ultrafast laser-induced magnetic relaxation in artificial spin ice driven by dipolar interactions, Phys. Rev. B **113**, 064404 (2026).

[35] S. A. Daunheimer, Reducing disorder in artificial kagome ice, Phys. Rev. Lett. **107**, 167201 (2011).

[36] Z. Budrikis, J. P. Morgan, J. Akerman, A. Stein, P. Politi, S. Langridge, C. H. Marrows, and R. L. Stamps, Disorder strength and field-driven ground state domain formation in artificial spin ice: Experiment, simulation, and theory, Phys. Rev. Lett. **109**, 037203 (2012).

[37] Z. Budrikis, P. Politi, and R. L. Stamps, A network model for field and quenched disorder effects in artificial spin ice, New J. Phys. **14**, 045008 (2012).

[38] J. M. Porro, A. Bedoya-Pinto, A. Berger, and P. Vavassori, Exploring thermally induced states in square artificial spin-ice arrays, New J. Phys. **15**, 055012 (2013).

[39] A. Farhan, P. M. Derlet, A. Kleibert, A. Balan, R. V. Chopdekar, M. Wyss, J. Perron, A. Scholl, F. Nolting, and L. J. Heyderman, Direct observation of thermal relaxation in artificial spin ice, Phys. Rev. Lett. **111**, 057204 (2013).

[40] X. Zhang, Y. Lao, J. Sklenar, N. S. Bingham, J. T. Batley, J. D. Watts, C. Nisoli, C. Leighton, and P. Schiffer, Understanding thermal annealing of artificial spin ice, APL Mater. **7**, 111112 (2019).

[41] B. Canals, I.-A. Chioar, V.-D. Nguyen, M. Hehn, D. Lacour, F. Montaigne, A. Locatelli, T. O. Menteş, B. S. Burgos, and N. Rougemaille, Fragmentation of magnetism in artificial kagome dipolar spin ice, Nat. Commun. **7**, 11446 (2016).

[42] R. F. Wang, J. Li, W. McConville, C. Nisoli, X. Ke, J. W. Freeland, V. Rose, M. Grimsditch, P. Lammert, V. H. Crespi, and P. Schiffer, Demagnetization protocols for frustrated interacting nanomagnet arrays, J. Appl. Phys. **101**, 09J104 (2007).

[43] J. P. Morgan, A. Bellew, A. Stein, S. Langridge, and C. Marrows, Linear field demagnetization of artificial magnetic square ice, Front. Phys. **1**, 28 (2013).

[44] X. Ke, Energy minimization and AC demagnetization in a nanomagnet array, Phys. Rev. Lett. **101**, 037205 (2008).

[45] F. Garcia, J. Sort, B. Rodmacq, S. Auffret, and B. Dieny, Large anomalous enhancement of perpendicular exchange bias by introduction of a nonmagnetic spacer between the ferromagnetic and antiferromagnetic layers, Appl. Phys. Lett. **83**, 3537 (2003).

[46] I. Theodorakos, I. Zergioti, V. Vamvakas, D. Tsoukalas, and Y. S. Raptis, Picosecond and nanosecond laser annealing and simulation of amorphous silicon thin films for solar cell applications, J. Appl. Phys. **115**, 043108 (2014).

[47] B. J. Simonds, S. Misra, N. Paudel, K. Vandewal, A. Salleo, C. Ferekides, and M. A. Scarpulla, Near infrared laser annealing of CdTe and in-situ measurement of the evolution of structural and optical properties, J. Appl. Phys. **119**, 165305 (2016).

[48] V. Scagnoli, Data supporting "Attaining the ground state of Kagome artificial spin ice via ultrafast site-specific laser annealing," [Data set], Zenodo (2025), doi:10.5281/zenodo.17967151.